ADVANCED
MATERIALS

Supporting Information

Programmable Self-Locking Origami Mechanical Metamaterials

Hongbin Fang,* Shih-Cheng A. Chu, Yutong Xia, and Kon Well Wang

Programmable Self-locking Origami Mechanical Metamaterials

Hongbin Fang*, Shih-Cheng A. Chu, Yutong Xia, Kon-Well Wang

Department of Mechanical Engineering, University of Michigan, Ann Arbor 48105, USA

Correspondence should be addressed to H. Fang (email: hongbinf@umich.edu)

I. Single-collinear (SC) origami kinematics

A. Single-collinear (SC) origami geometry and kinematics

Folding of the SC origami is a one-degree-of-freedom motion. To describe the geometry, two folding angles θ_1 and θ_2 are introduced as the dihedral angles between facets I, IV and the x-y reference plane (Figure S1). The x-y plane is constructed as follows: the x-axis is perpendicular to the parallel planes '1-2-3', '4-5-6', and '7-8-9'; the y-axis is determined such that the folding angles of facets I and II are equal (θ_1), and the folding angles of facets III and IV are also equal (θ_2). Hence, the external geometry of the SC origami can be expressed as [1]

$$h_i = a_i \sin\gamma_i \sin\theta_i,$$
(S1)

$$w_i = a_i \sqrt{1 - \sin^2\gamma_i \sin^2\theta_i},$$
(S2)

$$l_i = \frac{b_i \sin\gamma_i \cos\theta_i}{\sqrt{1 - \sin^2\gamma_i \sin^2\theta_i}},$$
(S3)

where the subscript i takes '1' or '2'. The two folding angles are not independent to each other but satisfy

$$\sin\gamma_1 \sin\theta_1 = \sin\gamma_2 \sin\theta_2.$$
(S4)

Hence, θ_1 can be assigned as the independent variable to describe the folding. For simplicity, we denote it as θ in what follows. When $\theta = 0°$, the SC cell is flat; when $\theta = 90°$, the SC cell self-locks because facets I and II bind together and are perpendicular to the x-y reference plane.
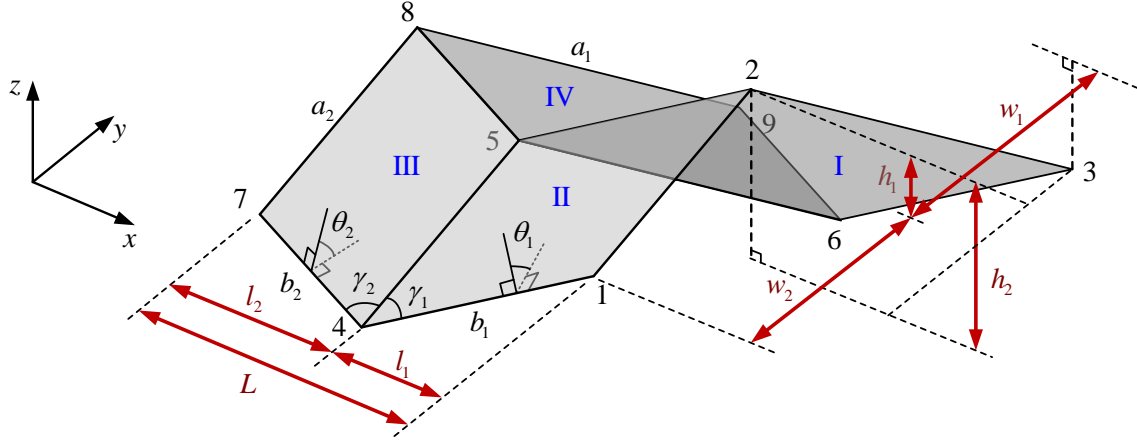
Figure S1. Geometry of an SC origami cell with crease lengths a_1, a_2, b_1, b_2, and sector angles γ_1, γ_2.

Then the length L of the SC cell can be determined as

$$L = l_1 + l_2 = b_1 \sin \gamma_1 \frac{\cos \theta + \beta \sqrt{\kappa^2 - \sin^2 \theta}}{\sqrt{1 - \sin^2 \gamma_1 \sin^2 \theta}},$$ (S5)

where $\beta = b_2 / b_1$ and $\kappa = \sin \gamma_2 / \sin \gamma_1$. Hence, at the initial flat state ($\theta = 0°$), the SC cell's length is

$$L_0 = b_1 \sin \gamma_1 + b_2 \sin \gamma_2;$$ (S6)

and at the self-locking configuration ($\theta = 90°$), the cell's length is

$$L_{SL} = \frac{b_2}{\cos \gamma_1} \sqrt{\sin^2 \gamma_2 - \sin^2 \gamma_1}.$$ (S7)

Then the SC cell's foldability can be calculated as

$$\eta = \frac{\Delta L_{max}}{L_0} = 1 - \frac{L_{SL}}{L_0} = 1 - \frac{\beta \sqrt{\sin^2 \gamma_2 - \sin^2 \gamma_1}}{\cos \gamma_1 (\sin \gamma_1 + \beta \sin \gamma_2)}.$$ (S8)

Two SC cells can be stacked together into a 3D cell (Figure S2), where the following constraints for compatibility need to be satisfied[1]

$$a_1^I = a_2^I = a^I, \ a_1^{II} = a_2^{II} = a^{II}, \ b_i^I = b_i^{II}, \ \frac{a^I}{a^{II}} = \frac{\cos \gamma_i^{II}}{\cos \gamma_i^I}, \ (i = 1, 2).$$ (S9)

Here the super-script '*I*' and '*II*' indicate the bottom SC cell '*I*' and the top SC cell '*II*', respectively. A chamber will be generated inside the stacked 3D cell. In this research, a special case that the 3D cell (in bulged-out configuration) is stacked by two identical SC cells is considered for kinematics study. Its enclosed volume can be obtained as [1]
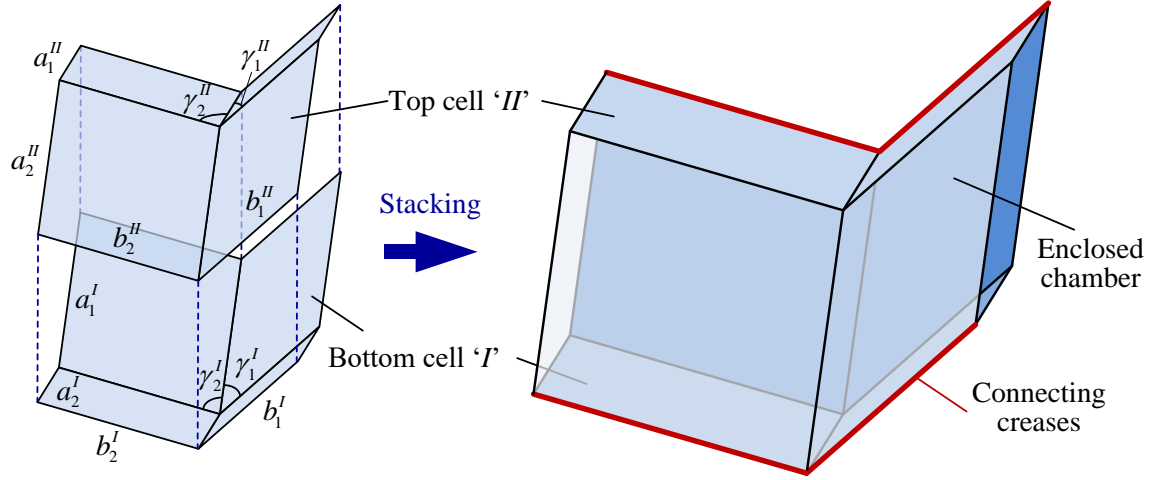
Figure S2. Stacking of two SC cells into a 3D unit and the generated enclosed chamber.

$$V = 2a_1a_2b_1 \sin^2 \gamma_1 \sin \theta \left(\cos \theta + \beta \sqrt{\kappa^2 - \sin^2 \theta} \right). \tag{S10}$$

The mass of all facets can be expressed as

$$m = 2\rho_F (a_1 + a_2)(b_1 \sin \gamma_1 + b_2 \sin \gamma_2), \tag{S11}$$

where ρ_F is the material surface density of the facets. The creases are assumed to be massless. Hence, the relative density of the 3D cell can be calculated as

$$\rho = \frac{m}{V}. \tag{S12}$$

At the self-locking configuration ($\theta = 90°$), the enclosed volume of the 3D cell is

$$V_{SL} = 2a_1a_2b_2 \sin \gamma_1 \sqrt{\sin^2 \gamma_2 - \sin^2 \gamma_1}. \tag{S13}$$

Substituting it into Equation (S12) yields the density at self-locking configuration, which can be further normalized by $\rho_F (a_1 + a_2)/a_1a_2$ into

$$\hat{\rho}_{SL} = \frac{\sin \gamma_1 + \beta \sin \gamma_2}{\beta \sin \gamma_1 \sqrt{\sin^2 \gamma_2 - \sin^2 \gamma_1}}. \tag{S13}$$

For $\beta = 0.5$ and $\beta = 2$, the foldability (η) of a SC cell (or a 3D cell) with respect to the sector angles γ_1 and γ_2 is shown in Figure S3a and S3b, respectively; the reciprocal of the normalized density ($1/\hat{\rho}_{SL}$) of the 3D cell at the self-locking configuration is shown in Figure S4a and Sb, respectively.
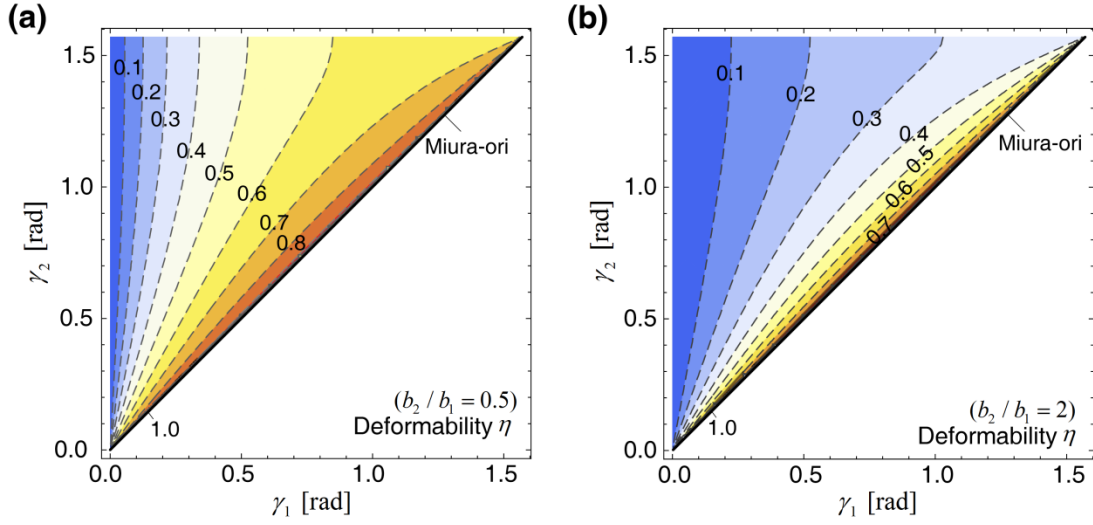
Figure S3. Achievable range of the foldability η with respect to the sector angles γ_1 and γ_2. Here (a) $b_2/b_1 = 0.5$ and (b) $b_2/b_1 = 2$, and the two constituent SC cells are identical. The symmetric part corresponding to $\pi/2 < \gamma_2 < \pi$ is omitted.
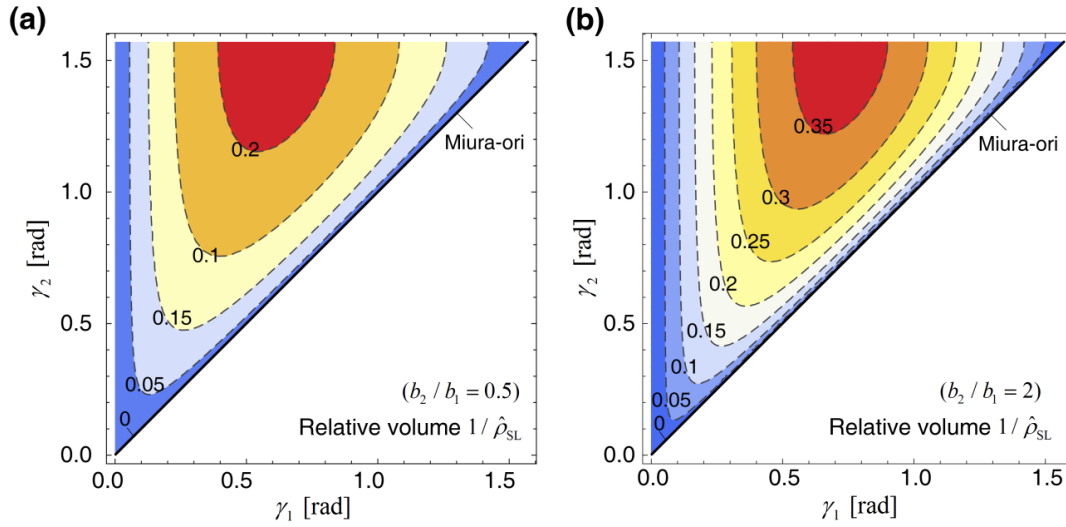

Figure S4. Achievable range of the normalized relative volume at the self-locking configuration $1/\hat{\rho}_{SL}$ (i.e., the reciprocal of the normalized relative density) with respect to the sector angles γ_1 and γ_2. Here (a) $b_2/b_1 = 0.5$ and (b) $b_2/b_1 = 2$, and the two constituent SC cells are identical. The symmetric part corresponding to $\pi/2 < \gamma_2 < \pi$ is omitted.

B. Heterogeneous construction of self-locking origami metamaterial

Degree-4 vertex cells of the same type but with different geometric patterns can also be connected together to achieve extra self-locking capability[2]. This research particularly focuses on the heterogeneous connection of Miura-ori cells; its kinematics is introduced in this section.
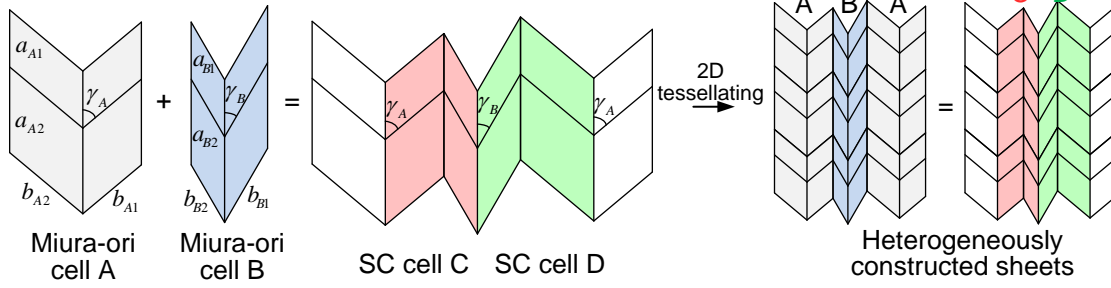
Figure S5. Heterogeneous construction of a self-locking sheet by connecting two different types of Miura-ori cells.

A schematic illustration of the 2D heterogeneous construction is shown in Figure S5, where each column is composed of identical Miura-ori cells (cell A or cell B), while each row is made up of cells with two different sector-angle assignments (cell A and cell B). Similarly, one sector angle (γ), two collinear-crease lengths (a_1 and α_2), and two zig-zag crease lengths (b_1 and b_2) are needed to describe the geometry of a single Miura-ori cell. Since each Miura-ori cell inherently possesses two collinear creases, two Miura-ori cells can be compatibly connected provided that the collinear-crease lengths satisfy the following geometry constraints

$$a_{A1} = a_{B1}, \ a_{A2} = a_{B2}. \tag{S12}$$

At the connections between cells A and B, SC cells C and D are generated.

Folding of the heterogeneously-constructed sheet can be determined by spherical trigonometry [2]. During folding, the newly generated SC cells cannot be folded flat, causing the overall sheet to lose flat-foldability. Without loss of generality, if assuming $\gamma_A > \gamma_B$, then in the whole sheet, the Miura-ori cells B can still be folded flat (the length of a Miura-ori cell B changes from L_{B0} to 0), while the Miura-ori cells A cannot be folded flat (the length of a Miura-ori cell A changes from L_{A0} to $L_{Af} \neq 0$) [2]. Hence, the foldability of the sheet can be obtained as

$$\eta = \frac{\Delta L}{L_{max}} = \frac{n_A(L_{A0} - L_{Af}) + n_B L_{B0}}{n_A L_{A0} + n_B L_{B0}}, \ (n_A \neq 0, \ n_B \neq 0), \tag{S13}$$

where n_A and n_B are the number of cells A and cells B in the sheet, respectively.

Figure S6 shows a 6-cell composed sheet made of two types of Miura-ori cell (cells A and B, with $\gamma_A > \gamma_B$). Here $n_A + n_B = 6$, $L_{A0} = 3.08$, $L_{B0} = 2$, $L_{Af} = 0.09 L_{A0}$. By adjusting the number of cells A and B (n_A and n_B), the sheet's foldability can vary within a large range.
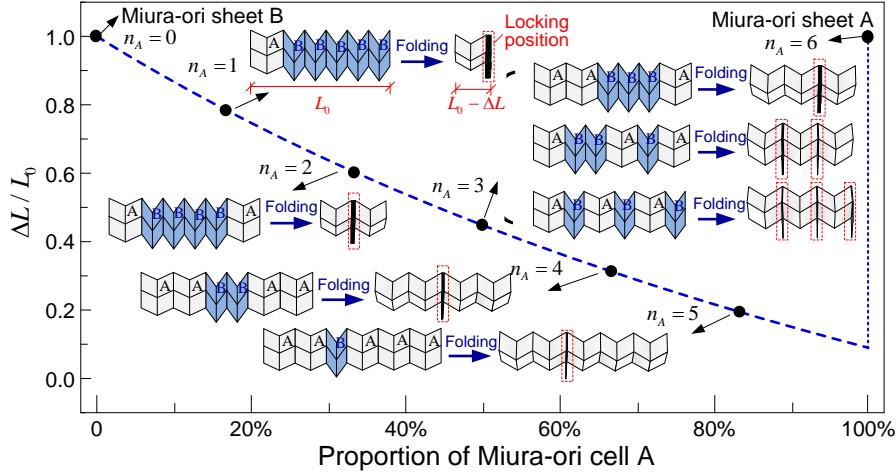
Figure S6. Self-locking metamaterials can also be heterogeneously constructed by connecting two types of Miura-ori cells. It provides a new approach to program the foldability.

Particularly, when $n_A = 0$ or $n_B = 0$, the sheet degenerates into the Miura-ori type and recovers flat-foldability. Moreover, with the same composition but different cell arrangements, the binding facets (i.e., the locking point) can occur at different positions, while the overall foldability remains unchanged. By exploiting this character in metamaterial development, the locking points can be reasonably arranged to optimize stress distribution.

Similarly, the 2D heterogeneous construction can be extended to the 3D scenario. In addition to the constraints for stacking two Miura-ori cells into a 3D cell (Equation (S6)), an additional constraint is required to compatibly connect two different 3D cells

$$\frac{\cos\gamma_{A1}^{I}}{\cos\gamma_{A1}^{II}} = \frac{\cos\gamma_{B1}^{I}}{\cos\gamma_{B1}^{II}}, \tag{S14}$$

where the superscript 'I' and 'II' denote the bottom cell 'I' and top cell 'II', respectively. At the connections between two different 3D Miura-ori cells, new 3D SC cells are generated. Since the self-locking kinematics of the 3D blocks is the same as the 2D sheets, results on the foldability (η) still work here and are not repeated.

II. Experiments

A. Prototype fabrication

Figure S7 shows the main steps for fabricating (a) the steel prototype, (b) the 3D-printed prototypes, and (c) the silicone elastomer prototype.

In the steel prototype (Figure S7a), 0.25mm-thick steel sheets (McMaster-Carr, product i.d.: 9011K271) are water-jet cut into parallelogram facet, and they are jointed via 0.13mm-thick adhesive-back ultrahigh molecular weight (UHMW) polyethylene film (McMaster-Carr, product i.d.: 1441T12). Pre-bent 0.10mm-thick spring steel stripes (McMaster-Carr, product i.d.: 9503K33) are pasted at the collinear creases of the top SC cell to provide certain stiffness for folding. The origami pattern geometry is given in Figure S7a.

3D-printing technology is also used for prototyping. Although there are many 3D-printing materials, certain flexibility is required to preserve the foldability. Here we print an Elasto Plastic (EP) prototype from Shapeways and a Flexible Photoreactive Resin (FPR) prototype from a Form-2 3D printer (Figure S7b). In this research, experimental studies on the locking-induced stiffness jumps are mainly based on the 3D-printed prototypes. To facilitate installation, supports are added to the 3D cell. The supports connect with the 3D cell through creases (Figure S8); their thicknesses are set to be 1 mm to reduce their influences on folding. Meanwhile, to investigate the effects of the crease thickness on the stiffness values, the collinear creases are set to be 1 mm, 2 mm, or 3 mm; all the other creases in the 3D cell are set to be identical in thickness, 1 mm. All facets of the 3D-printed origami prototypes are 5 mm in thickness.

At the other end of material stiffness, we can also use silicone elastomer (Mold Star 15 SLOW) and soft lithography technique to build soft self-locking origami with facet thickness 5mm and crease thickness 3mm (Figure S7c). The molds are designed in SolidWorks and fabricated through 3D printing (Form-2) with Black Photoreactive Resin. Before pouring into the silicone elastomer, a mist of mold release (Easy Release 200) is applied to all internal surfaces of the mold so that the prototype can be released readily from the mold. After casting the liquid elastomer in the mold at room temperature for more than 24 hours and demolding, we get the final prototype.
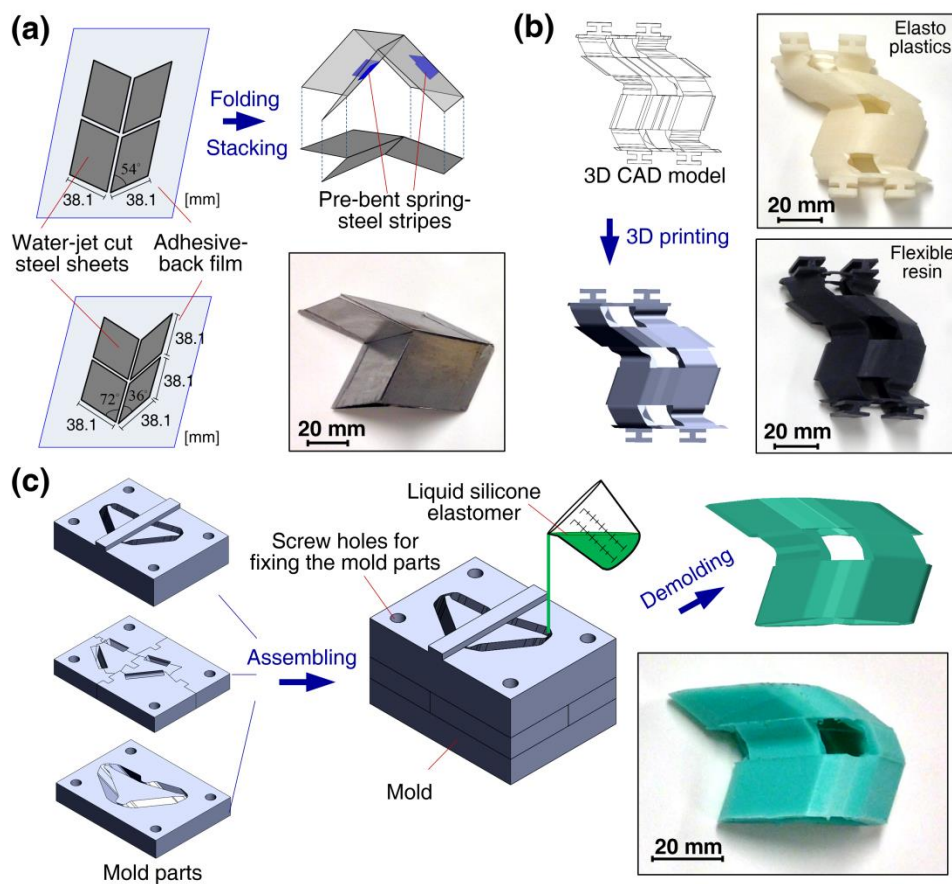
Figure S7. The main steps for fabricating a) the steel prototype (the SC pattern dimensions are given), b) the 3D-printed prototypes, and c) the silicone elastomer prototype.
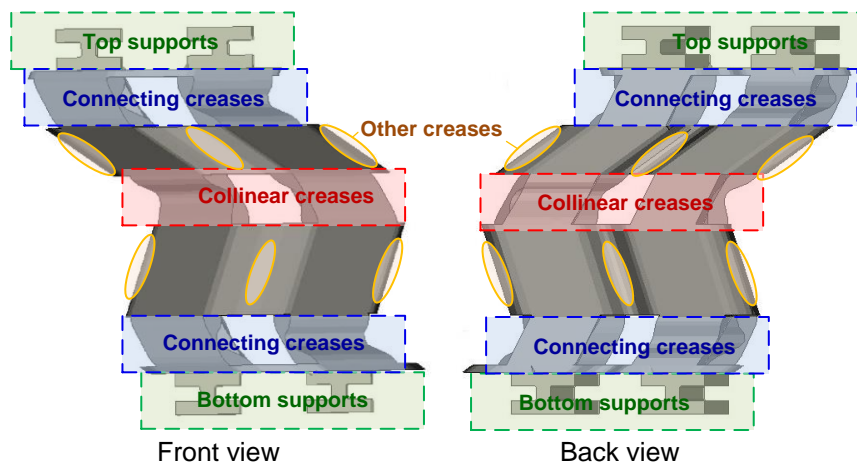

Figure S8. Geometry of the 3D-printed prototype. The thickness of the connecting creases and other creases are 1 mm; the thickness of the collinear creases is 1 mm, 2mm, or 3mm.

B. Material characterization

The material characteristics of the Elasto Plastics (EP) are provided by Shapeways. Due to the layer-by-layer production method, the tensile modulus of a 3D-printed EP part is direction dependent. The given tensile modulus in three directions is around 75MPa to 80MPa; the given Shore Hardness value is 35D.

The material characteristics of the Flexible Photopolymer Resin (FPR) are partially given by Formlabs. The given Shore Hardness value is 70-75A, which is much lower than that of the EP. This explains why the pre-locking and post-locking stiffness values of the FPR prototype are much lower than those of the EP prototype.

For the purpose of finite element (FE) analyses, the FPR's modulus is further determined through tests and approximation. Here the FPR is assumed to be compressible hyperelastic with rubber-like properties. Following the ASTM D575 standard testing procedures, a cylinder specimen of 28.6mm in diameter and 12.5mm in height is 3D-printed. It is then installed on the universal testing machine and compressed four times at the rate of 1mm/min. By importing the obtained stress-strain curves into Abaqus and based on the compressible Neo-Hookean model, the material constants C_{10} and D_1 can be obtained as: $C_{10} = 0.36$ and $D_1 = 0.40$. The Neo-Hookean model with these parameters is used in all FE analyses in this study.

C. Compression tests

Compression tests are carried out on the steel prototype, the EP prototype, and the FPR prototypes (with collinear-crease thickness 1 mm, 2mm, and 3mm). The steel prototype is placed between two slippery acetal resin sheets, onto which lubricating oil is also applied to guarantee the free folding of the steel prototype during compression (Figure S9a). The 3D-printed EP and FPR prototypes are first assembled with rigid plates, which are further fixed with the test tables (Figure S9b). These prototypes are compressed at the rate of 2mm/min. Figure S9 shows the photos of the three prototypes during compression tests at the initial pre-locking state, the locking point, and a post-locking state.

We also perform compression tests on the three-layer prototype. Figure S10 illustrates the experimental setup. The prototype is compressed at a rate of 5mm/min.
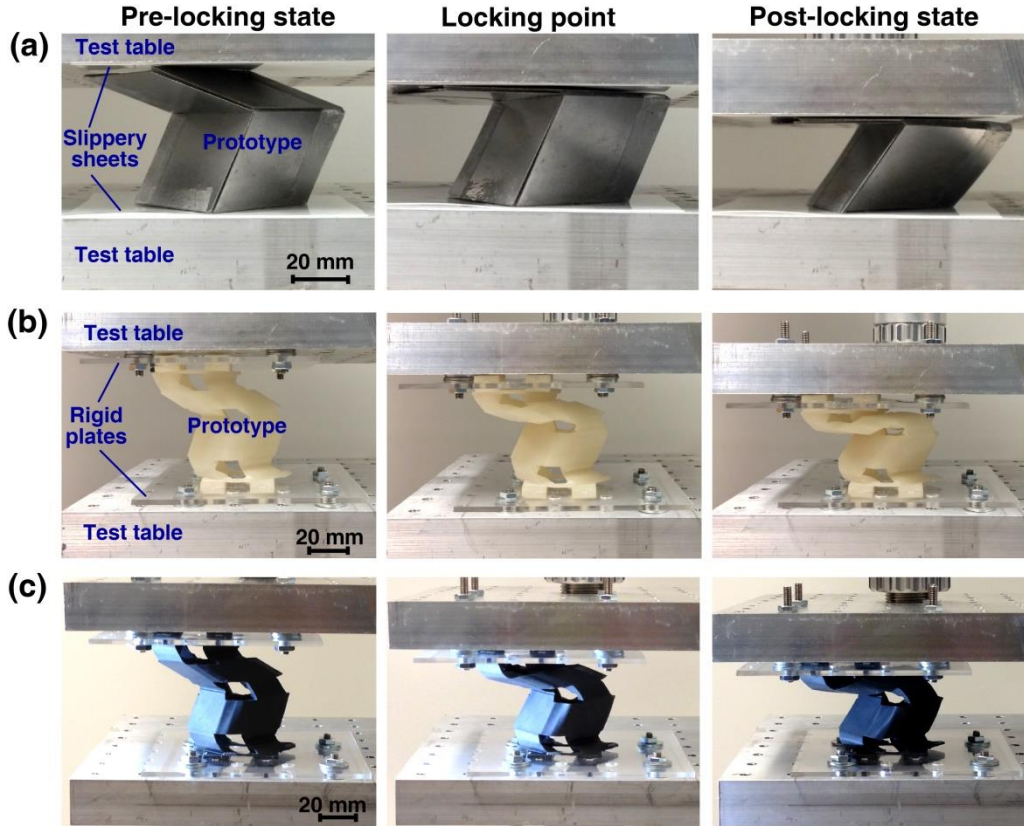
Figure S9. Photos of a) the steel prototype, b) the 3D-printed EP prototype, and c) the 3D-printed FPR prototype during compression tests. For each prototype, a pre-locking state (left), the locking point (middle), and a post-locking state (right) are shown. The experimental setups for the steel prototype and the 3D printed prototypes are illustrated in a) and b), respectively.
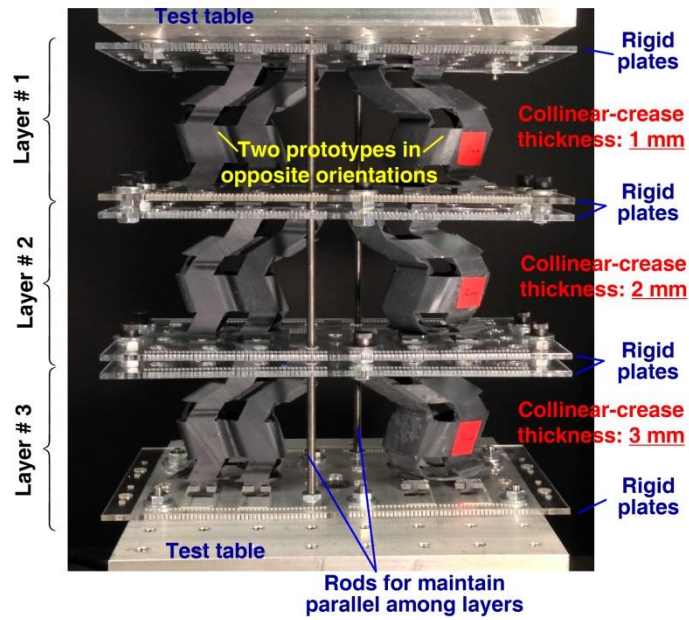

Figure S10. Setup of the three-layer prototype in compression tests.

III. Finite element analyses

A. Analysis setup

The finite element (FE) analyses are implemented using Abaqus to simulate the compression processes and the self-locking phenomenon. In all analyses, the 3D model is discretized using tetra-4 elements of side length 0.75mm (Figure S11). Hyper-elastic material is assumed for the FE analyses using the Neo-Hookean model, with $C_{10} = 0.36$ and $D_1 = 0.40$. To show the locking-induced effects, general contact is defined for the model, in which the contact domain includes all element-based surfaces.

In single-cell analyses, the bottom support panels are constrained in all degrees of freedom, and the top supports can only move downward in the vertical direction by bounding the nodes completely in all the other degrees of freedom (Figure S11a). Analyses under implicit quasi-static uniaxial compression are performed with displacement control acting on the top support panels.

In multi-layer analyses, the 1-mm cells (i.e., cells with collinear-crease thickness 1mm) are placed in the top layer (layer #1), the 2-mm cells are placed in the middle layer (layer #2), and the 3-mm cells are placed in the bottom layer (layer #3). The connections between cells in neighboring layers are rigidly constrained in all degrees of freedom except the vertical motion (Figure S11b). In the passive compression analysis, the bottom supports of the 3-mm cells are
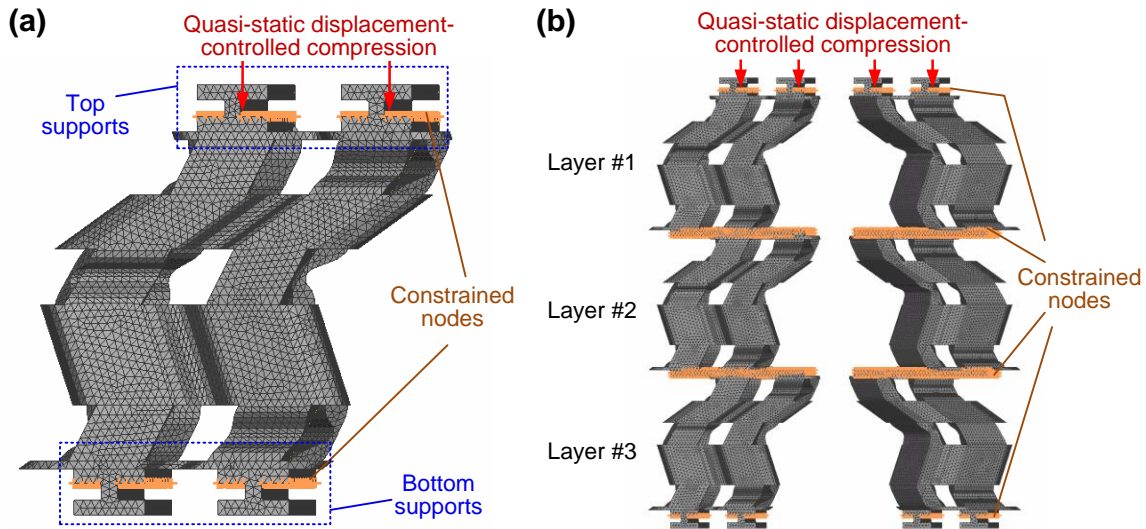

Figure S11. Finite element analysis setup for a) single-cell model and b) three-layer model.

constrained in all degrees of freedom, and displacement control is applied on the top supports of the 1-mm cells, which are constrained in all degrees of freedom except the vertical motion.

We also carry out FE analyses when cells in layer #2, layer #3, or both layers #2 and #3 are locked before regular compression. These analyses mimic the situations that the cells' configurations are on-line controllable via active folding mechanisms. To pre-compress the cells, an additional step is added before the regular compression steps. In detail, we apply forces on the target cells from their top and bottom supports; the magnitude of the force equals two times (because there are two cells to be pre-compressed) the critical force value when the single cell self-locks in the corresponding FE analysis. After the pre-compression step, the object cells would have already reached the locking state, and then the regular compression process applied at the top supports of the 1-mm cells will start.

B. Additional analysis results

Note that there is no difference in terms of FEA by placing the prototype upside, upside down, or horizontally because (a) a homogeneous material is used in the simulation; and (b) there is no gravity effect. However, Figure 2e reveals that the von Mises stress distributions of the top half and bottom half of the single cell are not uniform. The non-uniformity is induced by the different shapes and orientations of the facets. Referring to the model we studied in FEA, the facets of the top half are smaller than those of the bottom half, and during folding, the creases of the top half also rotate more than those of the bottom half, which explains why the stress of the top half is higher than that of the bottom half.

Figure S12 displays additional FE results. Figure S12a shows the stress distribution of the three-layer model under a passive compression. It reveals the same locking sequence as the experiment, i.e., the cells in layer #1 first lock, then the cells in layer #2 lock, and finally the cells in layer #3 lock. FE results corresponding to the cases with pre-compressed cells in layer #2, layer #3, and both layer #2 and #3 are shown in Figure S12b-d, respectively. In all these cases, the locking sequences agree with the corresponding experiments.
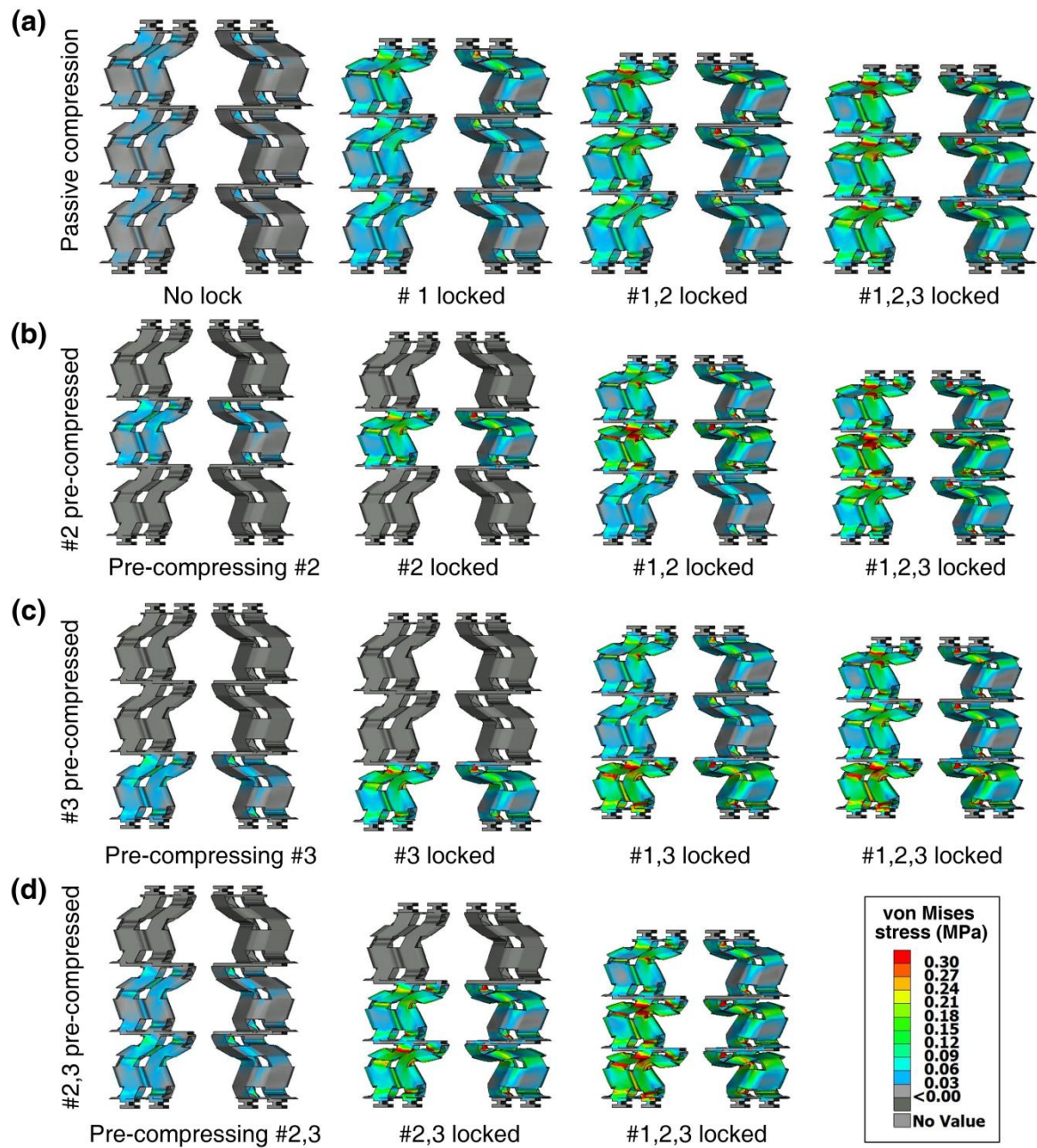
Figure S12. Additional FE results (stress-distribution) on the multi-layer model. a) Passive compression; b) cells in layer #2 are pre-compressed; c) cells in layer #3 are pre-compressed; d) cells in both layers #2 and #3 are pre-compressed.

IV. Equivalent model

A. Equivalent model and target stiffness

Based on the equivalent model of a single self-locking origami cell shown in Figure 3d in the main manuscript, the pre-locking and post-locking stiffness can be analytically expressed as

$$\begin{cases} k_{\text{pre-lock}} = k_1, \\ k_{\text{post-lock}} = k_1 + k_2. \end{cases} \tag{S15}$$

For the n-layer model, 2^n stiffness can be achieved. The two springs in each layer are connected in parallel, while the multiple layers are connected in series. Hence, the stiffness of each independent layer can be expressed as

$$K^i = \begin{cases} K^i_{\text{pre-lock}} = k_{i1}, \\ K^i_{\text{post-lock}} = k_{i1} + k_{i2}. \end{cases} \tag{S16}$$

Then the stiffness of the n-layer model yields

$$K = \sum_{i=1}^{n} \frac{1}{K^i}. \tag{S17}$$

Based on whether the i-th layer is locked or not, 2^n stiffness values can be obtained.

The above equations also work for target stiffness estimation. By approximating the pre-lock and post-lock stiffness from either experiments or FE analyses, the target stiffness can be obtained. Table S1 summarizes the experimental, FE, and prediction results; they are illustrated in Figure 3e of the main manuscript.

B. Error analysis

As mentioned in the main manuscript, qualitatively, the experimental/FE stiffness values agree well with the target stiffness. However, there are some quantitative discrepancies between the target stiffness and the measured/FE stiffness. The major reason for these quantitative discrepancies is the intrinsic nonlinearity originated from both the irregular geometry shape of the prototype and the material nonlinearity of the Flexible Photopolymer Resin (which is a rubber-like material). Although the linear fitting of the force-displacement curve is done with a high coefficient of determination, i.e., overall the linear model fits well with the measurement or analysis, the nonlinearity does induce different stiffness at different stages of compression. As is shown in Figure 2d, the slope of the force-deformation curve at the beginning stage of

pre-locking compression is higher than that at the ending stage of pre-locking compression. Such differences would be magnified in the multi-layer model, accounting for the discrepancies.

Table S1. Summarized results on locking-induced piecewise stiffness

	Experiment-based						FE Analysis-based					
Collinear crease thickness	**1mm**		**2mm**		**3mm**		**1mm**		**2mm**		**3mm**	
Stiffness-type	**Pre**	**Post**	**Pre**	**Post**	**Pre**	**Post**	**Pre**	**Post**	**Pre**	**Post**	**Pre**	**Post**
Values [N/mm]	0.269	1.239	0.489	1.416	0.756	1.516	0.333	1.080	0.558	1.501	0.758	1.673
Configuration	**No lock**		**#3 lock**		**#2 lock**		**No lock**		**#3 lock**		**#1 lock**	
Target stiffness [N/mm]	0.282		0.311		0.348		0.327		0.371		0.401	
Normalized target stiffness	1		1.103		1.233		1		1.134		1.226	

Table S1. Summarized results on locking-induced piecewise stiffness

	Experiment-based						FE Analysis-based					
Collinear crease thickness	**1mm**		**2mm**		**3mm**		**1mm**		**2mm**		**3mm**	
Stiffness-type	**Pre**	**Post**	**Pre**	**Post**	**Pre**	**Post**	**Pre**	**Post**	**Pre**	**Post**	**Pre**	**Post**
Values [N/mm]	0.269	1.239	0.489	1.416	0.756	1.516	0.333	1.080	0.558	1.501	0.758	1.673

Configuration	**No lock**	**#3 lock**	**#2 lock**	**#1 lock**	**No lock**	**#3 lock**	**#2 lock**	**#1 lock**
Target stiffness [N/mm]	0.282	0.311	0.348	0.479	0.327	0.371	0.401	0.495
Normalized target stiffness	1	1.103	1.233	1.697	1	1.134	1.226	1.514
Experimental-measured/ FE stiffness [N/mm]	0.348	/	/	0.398	0.369	0.358	0.408	0.495
Normalized value	1	/	/	1.144	1	0.970	1.106	1.341
Configuration	**#2,3 lock**	**#1,3 lock**	**#1,2 lock**	**#1,2,3 lock**	**#2,3 lock**	**#1,3 lock**	**#1,2 lock**	**#1,2,3 lock**
Target stiffness [N/mm]	0.393	0.570	0.705	0.920	0.469	0.603	0.687	0.913
Normalized target stiffness	1.394	2.018	2.498	3.261	1.433	1.844	2.100	2.792
Experimental-measured/ FE stiffness [N/mm]	/	/	0.684	1.128	0.412	0.529	0.650	1.142
Normalized value	/	/	1.966	3.241	1.116	1.433	1.760	3.095

V. Dynamics

A. Modeling and equation of motion

Here we develop the equation of motion of an origami metamaterial with bi-directional stop-limiting effect. For convenience, Figure S13a reproduces the sketch and equivalent model given in Figure 4b of the main manuscript. Detailed parameters for analytical and numerical investigations are given here. In the model, the absolute displacements of the lumped mass and the base are denoted by x and y, respectively. Hence, the relative deformation of the metamaterial is $(x-y)$. The base is subjected to harmonic base excitation $y(t)=Y\sin(\omega t)$, with amplitude Y and frequency ω.

Based on the equivalent model of a single self-locking cell, the metamaterial with symmetric bi-directional stop-limiting effect can be modeled as two cells connected in parallel. The two cells are pre-compressed before connecting with the lumped mass m so that each cell can be compressed or pulled by length d_1 without reaching the locking point or the flat state. During this interval ($-d_1 < x-y < d_1$), the equivalent stiffness of the structure is $2k_1$. When the left cell is compressed by more than d_1 (i.e., the right cell is pulled by more than d_1), the left cell enters the post-locking mode, which increases the stiffness to $2k_1+k_2$. Similarly, when the right cell is in post-locking mode, the stiffness is also increased to $2k_1+k_2$. If the deformation exceeds the limits ($x-y > d_1+d_2$ or $x-y < -(d_1+d_2)$), infinity stiffness is assumed. Hence, the force-deformation relation can be expressed as

$$F(x-y)=\begin{cases} 2k_1(x-y)+k_2(x-y+d_1), & -d_1-d_2 < x-y < -d_1, \\ 2k_1(x-y), & -d_1 < x-y < d_1, \\ 2k_1(x-y)+k_2(x-y-d_1), & d_1 < x-y < d_1+d_2. \end{cases} \tag{S18}$$

Then the governing equation of the system yields

$$\begin{cases} m\ddot{x}+F(x-y)+2c\cdot(\dot{x}-\dot{y})=0, \\ y=Y\sin(\omega t). \end{cases} \tag{S19}$$

where c denotes the equivalent viscous damping coefficient in each cell, which is assumed to be constant during the pre-locking folding and post-locking pressing modes.

On the other hand, the linear system used for comparison is governed by

$$\begin{cases} m\ddot{x}+F_L(x-y)+2c\cdot(\dot{x}-\dot{y})=0, \\ y=Y\sin(\omega t), \end{cases} \tag{S20}$$
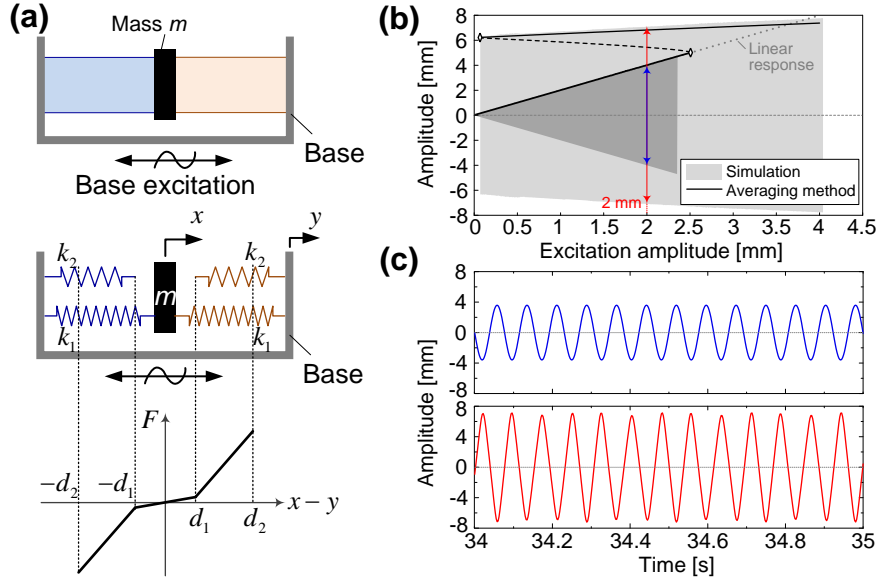
Figure S13. Dynamic analyses. a) Schematic illustrations of a bi-directional limiting-stopper metamaterial under base excitations and its equivalent dynamic model. b) The relative displacement responses with respect to different excitation amplitude at frequency 13 Hz. The light and dark grey represent the coexisting responses with high and low relative displacement amplitudes at the same excitation; the solid curves indicate the analytical prediction based on the method of averaging, and the dashed curve indicates the unstable solution; the responses of the corresponding linear system is denoted by the dotted curve. The bifurcation point is denoted by the diamond marker. c) Characteristic low-amplitude (top) and high-amplitude (bottom) time-histories of the relative displacement of the lumped mass under harmonic base excitation with amplitude 2 mm and frequency 13 Hz.

where the linear force-deformation relation F_L is

$$F_L(x-y) = 2k_1(x-y).$$ (S21)

B. Numerical Analyses

In this research, the relative displacement-excitation relations are numerically and analytically investigated. The method of averaging is an effective method to analytically solve this kind of system with piecewise stiffness profile [3,4].

As an example, the following parameters are used for numerical studies: $m = 0.3\,\mathrm{kg}$, $c = 0.1\,\mathrm{N \cdot s/m}$, $k_1 = 0.5\,\mathrm{N/mm}$, $k_2 = 10\,\mathrm{N/mm}$, $d_1 = 5\,\mathrm{mm}$, and $d_2 = 15\,\mathrm{mm}$. For real prototypes, these parameters can be obtained from the static experiments or FE analyses. When solving the amplitude-frequency relation, the excitation amplitude Y is set as 2 mm, and the frequency is discretely scanned from 5 Hz to 25 Hz, with step 0.2 Hz. To capture all possible

dynamics, 100 initial conditions are randomly taken among the region $[-2,2]\,(\text{mm})\times[-2000,2000]\,(\text{mm/s})$ at each frequency. This gives rise to the numerical amplitude-frequency response diagram shown in Fig. 4c of the main manuscript. On the other hand, with fixed excitation frequency at 13 Hz, we discretely scan the excitation amplitude from 0.01mm to 4mm, with step 0.01mm. Similarly, we take 100 initial conditions to capture various possible responses. The relative displacement responses of the lumped mass with respect to different excitation amplitudes are shown in Figure S13b, which also exhibit dynamically bistable oscillations (e.g., Fig. S13c shows two characteristic time histories of the relative displacement when the excitation amplitude is 2mm).

References

[1]   S. Li, H. Fang, K. W. Wang, *Phys. Rev. Lett.* **2016**, *117*, 114301.
[2]   H. Fang, S. Li, K. W. Wang, *Proc. R. Soc. A Math. Phys. Eng. Sci.* **2016**, *472*, 20160682.
[3]   X. Shui, S. Wang, *Mech. Syst. Signal Process.* **2018**, *100*, 330.
[4]   A. Narimani, M. E. Golnaraghi, G. N. Jazar, *J. Vib. Control* **2004**, *10*, 1775.